Zhang Xi (Orcid ID: 0000-0002-3313-8095)
Zhang Fengshou (Orcid ID: 0000-0002-4998-6259)

Changes of slip rate and slip-plane orientation by fault geometrical complexities during fluid injection

Xi Zhang[1,*], Bisheng Wu[2], Robert G. Jeffrey[3], Diansen Yang[4], Weizhong Chen[4], Fengshou Zhang[5]

[1] CSIRO Energy, Melbourne, Australia

[2] State Key Laboratory of Hydroscience and Engineering, Department of Hydraulic Engineering, Tsinghua University, Beijing, China

[3] SCT Operation Ltd., Wollongong, Australia

[4] State Key Laboratory of Geomechanics and Geotechnical Engineering, Institute of Rock and Soil Mechanics, Chinese Academy of Sciences, Wuhan, China

[5] Department of Geotechnical Engineering, Tongji University, Shanghai, China

[*] Corresponding author: Xi. Zhang (xi.zhang@csiro.au)

Key Points:

1. Along-the-fault geometrical complexities affect the slip location and rate.
2. Short-term fast slip rates can be generated by along-the-fault dilational segments.
3. Fast slip duration and spatial pattern from seismicity may provide an estimate of rupture geometries.

This article has been accepted for publication and undergone full peer review but has not been through the copyediting, typesetting, pagination and proofreading process which may lead to differences between this version and the Version of Record. Please cite this article as doi: 10.1029/2019JB017856

Abstract

[1] The injection-induced slip of a fault containing along-the-fault geometrical complexities such as permeable cracks, dilational jogs and branches, was studied numerically using a plane-strain hydraulic fracture model. The fault is modelled by placing complexities evenly spaced on either side of the inlet where fluid coming from a steady source is injected at a constant rate. The fault slip obeys the Coulomb friction law with slip weakening of the coefficient of friction. The applied shear stress is less than the residual fault strength, corresponding to a situation where a fault undergoes stable slip behind a slowly advancing rupture front. The numerical results show that the segments of complexity may not only delay slip zone extension and fluid flow, but temporarily increase slip rates. Short-term faster slip rates occur after cracks and jogs are pressurized. The slip rate can reach values typical of micro-earthquake events, accompanied by rising and then dropping pressure and producing a stress release. Especially, the discontinuous slip sources are separated by the right-angle jogs that do not slip. The slip on branches can be activated by fluid invasion and an associated normal effective stress reduction, and the slow slip sources eventually move from the fault to the branches. Even if a hydraulic fracturing treatment presents a low risk of generating dynamic slip, when fractures intersect faults containing geometrical complexities, fast slip events may be induced. The spatio-temporally varying slip rates and patterns presented provide an alternative interpretation for recorded seismic slip signals.

Keywords: fluid flow along a fault, segments rupturing coherently, hydraulic fracture model, transient slip patterns, permeability changes

1. Introduction

[2] A growing body of evidence of seismicity indicates that fluid flow and rupture growth are intimately linked to fault permeability for faults subject to fluid injection. The injection of fluid may occur when a fault is connected to an overpressurized fluid source, either natural or from human activities [*Ellsworth*, 2013; *Bao* and *Eaton*, 2016]. Elevated fluid pressure and its diffusion through a rock mass can pressurize faults, activating fault slip by decreasing the effective normal stress acting across the fault, which is calculated by subtracting the pore pressure from the confining stress. In some cases such as low-permeability reservoir stimulation, waste injection and geothermal extraction, the permeability that allows fluid flow can originate from hydraulic fractures, which are extended by fluid pressures that exceed the least compressive stress [*Hubbert and William*, 1959; *Cox*, 1995]. Hybrid tension-shear fracture growth can occur that creates progressively enhanced permeabilities along the plane of the growing fracture [*Šílený et al.*, 2009; *McClure and Horne*, 2011; *Guglielmi et al.*, 2015; *Galis et al.*, 2017]. Apart from the opening caused by overpressure, pre-existing faults and natural fractures can also act as fluid conduits. In nature, many pre-existing faults are originally formed as dilational fractures [*Segall* and *Pollard*, 1983] or cracks and their hydrological features would be different. Here we focus on shallow poorly developed faults [*Caine et al*., 1996], which have a number of thin fractures with various apertures across the fault zone and this composite permeable fracture system is typically modeled as a single fracture conduit with parallel walls. Fault permeability is not uniform, but heterogeneous along the fault length, and when subject to fluid injection this variation in permeability results in a non-uniform fault strength. The contribution of elevated pressure and fluid flow to rupture growth has received a great deal of attention [*Rutledge et al.*, 2004; *Jeffrey et al.*, 2009; *Warpinski*, 2014; *Zhang and Jeffrey*, 2014; *Zhang, Damjanac, et al.*, 2019]. Although the rupture location and timing is recognized as being linked to it [*Boatwright*, 1984; *Sibson*, 1986, 2000; *Urbancic* and *Trifu*, 1996], the effect of the geometrical heterogeneity on slip and pressurized zone development during fluid injection has not been fully explored.

[3] The slip responses along a permeable fault during fluid injection do not follow the trend seen in earthquakes where seismicity follows a decaying main shock-aftershocks pattern. Instead, the injection-induced slow slip is generated that is associated with swarm-like seismicity that expands outwards from the injection point and occurs over a long period of time [*Rutledge et al.*, 2004; *Shapiro et al., 200*6; *McClure and Horne*, 2011; *Zoback et al.*, 2012; *Das and Zoback*, 2013]. Quantification of the coupled fluid migration and shearing

along permeable faults is thus recognized as critical for understanding injection induced seismicity and the potential for dynamic, unstable slip nucleation. The nucleation of dynamic slip from a constant permeability fault or a fault that is opened by the injected fluid has been investigated [*Garagash and Germanovich*, 2012; *Viesca and Rice*, 2012; *Azad et al.*, 2017], revealing the importance of lower shear stress environments and a smaller opening zone on reducing the likelihood of unstable fault slip events. On the other hand, the permeability changes occurring during dilatant hardening can produce a slow slip response that also is associated with the absence of dynamic slip nucleation even if the applied shear stress is larger than the residual frictional strength of the fault [*Zhang et al*., 2019; *Ciardo and Lecampion*, 2019]. From these studies, it is expected that fault permeability generated by pre-existing geometrical complexities (GCs) may also be an important contributing factor leading to the observed slip responses during fluid injection.

[4] The pre-existing permeable fault GCs, acting as a pressure sink, can result in a variety of slip patterns and their effects on changing the slip rate and causing re-orientation of the slip plane are both areas requiring more study. Most faults have a non-planar geometry, which can lead to additional forces arising during shear slip events and the associated variation of aperture during shearing may act to reduce or enhance fluid flow compared to shear-induced deformation along flat faults. In the presence of GCs, the interaction between pressure and slip becomes more complicated, and dynamic slip events can lead to stress release [*Boatwright*, 1984; *Urbancic* and *Trifu*, 1996; *Sibson*, 2000]. For example, one result of the varying stresses can be progressive slip development along non-planar branches or along secondary fractures [*Segall and Pollard*, 1983; *Petit et al.*, 1999]. In addition, the strong slip events that occur provide an indication of the existence of compressive and dilational jogs along the fault [*Rutledge et al*., 2004]. Such jogs have been found in large volcanic calderas, on the edges of which the pressurized magma has generated slip along sections of faults containing pre-existing jogs [*Waite and Smith*, 2002; *Shelly et al.*, 2013; *Shelly et al.*, 2016a]. Rupturing in fact is not a simple process of frictional slip failure along a planar surface with homogeneous frictional and permeability distributions. Cracks, jogs (also called step-overs) and branches along the fault patch, generating hydraulic conductivity, have been recognized as important structural features in natural and man-made fracturing processes that locally cause stress changes [*Segall and Pollard*, 1983; *Sibson*, 1986; *Cox*, 1995; *Urbancic and Trifu*, 1996] and swarm-like seismic events associated with the slip [*Rutledge et al.*, 2004; *Shelly et al.*, 2016b].

[5] Three common sorts of fault GCs will be considered in this paper; (1) unconnected parallel fractures or cracks, (2) parallel fractures connected by jogs or offsets, and (3) fracture branches or splay fractures. A fault system often contains multiple unconnected parallel fracture segments with or without offsets [*Segall and Pollard*, 1983]. The segment interaction under shear loading will generate high stress, leading to damage zones, where the parallel segments join. The permeability of these damage zones or cracks, which form dilational segment as discussed by *Aki et al*. [1977], *Sibson* [1986] and *Yamashita* [1997], is much larger than that of the original permeability of the connected segments. If no offsets exist between parallel fractures, the high-permeability zone acts as a co-planar fracture array, and otherwise, it is described as a zone of dilational jogs in many studies [*Sibson*, 1986; *Rutledge et al*. 2004; *Jeffrey et al.*, 2009]. The cracks and jogs exist with a range of length scales in their extent ranging from millimeters to kilometers [*Sibson*, 1985]. The third sort of GCs consist of branches and non-planar splay fractures that deviated from the fault plane [*Cooke*, 1997; *Segall and Pollard*, 1983; *Petit et al.*, 1999; *Zhang and Jeffrey*, 2016]. The branching fractures also exist with a wide range of sizes and permeability [*Yamashita*, 1997]. These GCs can slip and dilate, and be pressurized by fluid [*Phillips*, 1972; *Petit et al.*, 1999; *Sibson*, 2000]. The slip front may propagate far away from the fluid sources, assisted by pressurized fluid in accordance with stress equilibrium, frictional strength and sliding kinematics.

[6] Although the GCs may modify the fault surface features that would change the local fault shear strength, a unified friction law for predicting the along-the-fault slip is generally used in the models for simplicity. The slipping process on a shallow fault pressurized by a hydraulic fracture treatment produces the slip speed that is normally slow prior to the onset of unstable dynamic slip [*Das and Zoback*, 2013; *Guglielmi et al*., 2015]. For a stable slow slip process, frictional strength of a fault can be characterized by the slip weakening friction law [*Uenishi* and *Rice*, 2003]. The linear weakening form of the coefficient of friction with slip, as presented by *Ida* [1972] can provide a first-order approximation for the slip response [*Uenishi* and *Rice*, 2003]. Slip weakening is implemented as a displacement-dependent Coulomb friction law that has been found to be useful and numerically efficient [*Marone et al*., 1992; *Yamashita*, 1997]. Based on the previous studies on injection-induced dynamic slip nucleation [*Viesca and Rice*, 2012; *Garagash and Germanovich*, 2012; *Azad et al*., 2017; *Zhang et al*., 2019; *Ciardo and Lecampion*, 2019], the linear slip weakening friction law allows initially stable slip to develop into unstable slip and produces a variety of responses for evolution of the slip and slip zone on a permeable or impermeable fault.

[7] The mechanical interaction between pressure diffusion and fault slip is a key to understanding the transition from stable aseismic to unstable dynamic slip since fault strength varies. When the slip-weakening friction law is used, the slip regime is dependent on whether the applied shear stress is less than the residual frictional strength or not. In the former case the slip rate evolution can enter into an ultimately stable regime so that the aseismic slip persists [*Garagash and Germanovich*, 2012]. Clearly, this stable slip state, however, can be perturbed or broken by other sources of permeability change, such as fault GCs that result in non-uniform fault strength. In fact, the effects of shearing dilational segments have been long recognized as the main driving force for the generation of small earthquakes [*Aki et al.*, 1977; *Rutledge et al.*, 2004; *Shelly et al.*, 2016a]. Dilation of part of the fault can disturb the stable slow slip processes by increasing slip rates and producing micro-earthquake events. It is necessary to explore the mechanisms for generating these small events, which are associated with fluid pressure variations at locations on the fault that contain GCs.

[8] In this paper, we consider slip development affected by GCs along an undrained fault. The fault is pressurized by injected fluid, possibly from a hydraulic fracturing stimulation of a low-permeability gas reservoir, where the reservoir pore pressure influence is ignored. Along the fault trace, multiple GCs in one of the three sorts mentioned above are distributed symmetrically on both sides of the injection point. The loading conditions used result in stable slow slip on a simple planar fault, but the existence of these complexities interacting with the fluid pressure, perturbs the stable slow slip. A hydraulic fracture simulator with fully coupled fluid flow and fracture deformation [*Zhang et al.*, 2009; *Zhang and Jeffrey*, 2014] is used to explicitly track the moving fronts of the opening, slipping and pressurized zones. The accelerated slip rate is a few orders of magnitude higher than the aseismic slip rate (<0.001 mm/s), but it is much smaller than 1m/s, a typical earthquake slip speed used for small events [*Lapusta et al.*, 2000]. In addition, the storage capability of the dilational segments is limited and their aperture is much smaller than their length so that fluid flow within them can still be described in the framework of discrete fractures with parallel walls. The physical model is presented in section 2, followed by the main numerical results and discussion for slip rate variations caused by three different GCs and coefficients of friction. In the end the paper is concluded by a summary of the findings.

2. Model

2.1 Problem statement

[9] We consider the slip zone growth along an infinite fault in a homogeneous, isotropic and linearly elastic rock, driven by the pressurized fluid injected at a constant rate. During a hydraulic fracturing treatment in a low-permeability reservoir, a nearby fault can be connected to the injection zone in several ways. For example, an opening-mode hydraulic fracture may grow directly into the fault over a period of injection time [*Ellsworth*, 2013], and several fracture treatments may intersect a fault sequentially. In this study we do not consider details of the connection process. We also make the following simplifying assumptions:

[10] (1) The fault is immature and treated as discrete conduits with parallel walls [*Caine et al*., 1996] and the surfaces of the fault are sealed [*Blanpied et al*., 1993]. The dominant nature of along-the-fault fluid flow has been used in many previous studies [*Yamashita*, 1997; *Viesca and Rice*, 2012; *Garagash and Germonovich*, 2012; *Zhang et al*., 2019], in contrast to the mature fault zone model with an inner low-permeability core and surrounding high-permeability damage zones [*Wibberley and Shimamoto*, 2002]. The dilational GCs, which are of relatively larger permeability compared to the overall fault permeability, also follow this assumption.

[11] (2) The injection rate is constant and the flow rate along the fault is small enough so that turbulent effects and any shear stress on the fracture walls generated by viscous fluid flow and surface roughness can be neglected.

[12] (3) Rock deformation is plane-strain and the fracture dimension in the out-of-plane direction is of a size much larger than other dimensions. The general fracture deformation and internal pressure states along a straight fault are illustrated in Fig. 1. The normal stress across the fracture walls is positive in compression, while the shear stress is considered as positive if the top-bottom pair of shear tractions tends to spin the body anti-clockwise as shown in Fig. 1. In contrast to pure shear crack models, the fault can be opened by elevated fluid pressure, and thus hybrid shear slip and opening may co-exist at one location.

[13] As shown in Fig. 1, the fault surface can be partially supported by fluid pressure (p) in the zone filled by fluid. On parts of the fault that are not fully opened, a contact traction (σ_n) and a shear traction (τ) act. In the opening zone, the pressure is large enough to open the fault surfaces and the contact and shear tractions are equal to zero. The tractions acting on

the fault walls are balanced by the background normal (σ_0) and shear (τ_0) stresses, which are imposed on the fault surface by the remote stresses. The resulting fracture wall displacements are denoted by the opening (*w*) and shear (*u*) displacement discontinuities (DDs). The pressure, tractions and DDs are functions of time and location. In addition to fault opening, the pre-existing hydraulic conductivity, in terms of hydraulic aperture [*Brown*, 1987], also contributes to pressure diffusion along the fault. The hydraulic aperture is denoted by *e* in Fig. 1, which is comparable in magnitude to fault opening at the GCs.

[14] Based on the pressure diffusion and rock deformation, the problem considered involves an opening front (l_0) where the opening zone ends and the slip front (l_s) where the currently active slip zone ends, as shown in Fig. 1. The fluid movement into a conductive fault portion results in the fluid front (l_f), which can be located at a position different from the other fronts. A fluid lag zone exists if the slip or opening front is ahead of the fluid front. The lag zone was recognized and discussed in previous studies [*Scotti and Cornet*, 1994; *McClure and Horne*, 2011; *Gugilielmi et al*., 2015].

[15] The real distributions of GCs along a fault can be extremely complicated because they are created by tectonic loading. Here we focus on the effects of GCs on fault slip development. For the problems to be tractable, we consider three simple geometries as shown in Figs. 2(a-c). One type of dilational segment is used for each geometry and the four segments are symmetrically distributed along the fault on both sides of the injection point, where fluid enters the fault. The first case considered is as shown in Fig. 2(a), consisting of a chain of four cracks with relatively higher permeability than the main fault, which connects them to the fluid source. This geometry was used by *Aki et al*. [1977] for investigating the mechanism responsible for volcanic tremors. The second case, as shown in Fig. 2(b), consists of four en echelon fractures forming dilational jogs [*Segall and Pollard*, 1983]. The jogs are important to many geological processes and can be a site of seismic and aseismic slip, hydrocarbon migration and entrapment, and conduits for mineralizing fluids [*Sibson*, 1986; *Cox*, 1995; *Urbancic and Trifu*, 1996; *Rutledge et al*. 2004; *Fielding et al.*, 2009; *Micklethwaite*, 2009; *Shelly et al.*, 2016a]. The third case considered consists of four oblique fault branches as shown in Fig. 2(c), due to the tensile, fault-parallel normal stress, σ_t, which may arise along the top surface of the fracture near the slip zone end [*Cooke*, 1997; *Petit et al.*, 1999]. Branch fractures are assumed to have formed off the fault plane on the extensional

side and are evidence that a shear-induced tensile stress is large enough to create tensile fractures once existed there [*Zhang and Jeffrey*, 2016]. Outside the four segments, the fault is assumed to be parallel to the *x* axis, even though there is an offset caused by jogs as shown in Fig. 2(b).

[16] The geometrical parameters for each case are labelled in Fig. 2, including the distance between two complexities, *c*, the size of dilational segments, *a*, the size of branches, *b*, and the angle, θ, between the branch or the oblique parts and the main fault plane which lies along the *x*-axis. The sizes of the GCs may vary over several orders of magnitude [*Sibson*, 1985], while the permeability of natural faults ranges over 10 orders of magnitude [*Caine et al*., 1996]. For shallow faults considered, the segment lengths are on the order of meters [*Sibson*, 1985], but the length scale can be much less in lab tests [*Ye and Ghassemi*, 2018]. In the computations, we use c= 4m for three cases, and a=0.4m in Figs. 2(a) and (b). We impose no limit on branch size and do not consider the effect of small branch size and fracture re-initiation. A case study by *Rutledge et al*. [2004] also suggests that steps and jogs vary in length. Although we use the meter-scale complexities, it must be mentioned that some fine-scale complexities can also affect slip and flow behaviors. In addition, the hydraulic aperture, *e*, is assumed to be less than 0.5mm for the dilational segments and other portions are set to apertures of 0.01 mm if not otherwise specified. This choice ensures that the widely-used cubic law [*Zimmerman and Bodvarsson*, 1996] be valid for fluid flow in closed fracture sections because the aperture is much smaller than the length used.

[17] To better present the slip and pressure evolution in time, we have specified five locations along the fault, labelled A, B, C, D and E in order from left to right as shown in Figs 2(a-c). By taking advantage of the geometric symmetry, only the results for half the fault system needs to be reported. Point A is at the mid-point between the inlet and the first complexity adjacent to the inlet. Point B is at the mid-point of the first crack and jog in Figs. 2(a) and (b) or is the location on the first branch at a distance of d=1m to the intersection in Fig. 2(c). Point C is at the mid-point of the fault segment between the two complexities, and point D is at the mid-point of the second crack and jog, as shown in Figs. 2(a) and (b) or is at the location on the second branch at a distance of 0.15d to the intersection as shown in Fig. 2(c). Point E is the point on the main fault at a distance of c/2 from the end of the second dilational segment as shown in Fig. 2(a), but at 0.1c as shown in Fig. 2(b) and at 0.25c to the second intersection as shown in Fig. 2(c).

[18] The remote stress conditions considered are provided in Fig. 2(d), highlighting the

mismatch between the fault plane orientation and the principal stress directions. The remote normal stress condition $\sigma_{yy} = \sigma_{xx}$ implies that the principal stress direction is at 45 degrees with respect to the *x* axis. The acting principal stresses are denoted by σ_1 and σ_2, which are transformed to the fault direction to obtain the normal and shear stress components acting on the fault segments that may be oriented at an angle to the x-axis. For the cases studied, the remote shear stress τ_{xy} is 4MPa if not otherwise specified and the remote normal stresses σ_{xx} and σ_{yy} are both 10MPa. As discussed below, this remote stress condition is such that a stable slow slip condition is maintained for a planar fault lying along the *x* axis in the absence of complexities. Hence, the focus of the numerical study is on the effects of GCs in modifying slip and pressure transients.

[19] Apart from geometric and loading settings, we make some simplifications in selecting suitable controlling equations for fault deformation and fluid flow. They are summarized for completeness as: (1) negligible poroelastic and plastic effects other than the plastic effect inherent in frictional sliding exist on the fault surfaces, and no flow perpendicular to the fault surface; (2) weakening of frictional strength occurs only by slip amount, stress change and pressure increase and the same friction law is used over the fault including complexities although their presence can create a frictional strength barrier that acts to resist slip; (3) plane-strain quasistatic shear crack growth is modelled at slow slip rates; (4) small pre-existing hydraulic apertures exist representing an immature fault zone.

2.2 Linear elasticity

[20] To account for the stress equilibrium of a fault, the equations of equilibrium [*Zhang et al.*, 2009] provide the relationship between and the tractions, including the fluid pressure p, and DDs along the fault. For the slow slip process studied, seismic wave and inertia effects are not included. As a reference, the slip rate for smaller tectonic events is around 1m/s [*Lapusta et al*., 2000). Here the slip rate considered is much less than this reference value for the fault given the remote shear stress and residual frictional strength. A quasistatic model is suitable and commonly used for studying injection-induced slip [*Das and Zoback*, 2013; *Guglielmi* et al., 2015].

[21] If the problem contains *N* fracture segments, the elasticity equations in the Cartesian coordinate system for the three cases shown in Fig. 2 are

$$\sigma_n(\boldsymbol{x},t) + p(\boldsymbol{x},t) - \sigma_0(\boldsymbol{x}) = \sum_{i=1}^{N} \int_0^{l_i} [G_{11}(\boldsymbol{x},s)w(s,t) + G_{12}(\boldsymbol{x},s)u(s,t)]\mathrm{d}s \quad (1)$$

$$\tau(\boldsymbol{x},t)-\tau_0(\boldsymbol{x})=\sum_{i=1}^{N}\int_0^{l_i}[G_{21}(\boldsymbol{x},s)w(s,t)+G_{22}(\boldsymbol{x},s)u(s,t)]\mathrm{d}s \tag{2}$$

where $\boldsymbol{x}=(x,y)$ gives the coordinates of a point on the fault system that includes GCs and *t* is time staring from the instant when the fluid is fed into the fault. *s* is the arc length along the fault and l_i is the length of the fault segment *i*. The shear traction τ on the fault surface originates from the frictional stress. The integrand G_{ij} (*i*, *j*=1,2) are the hypersingular Green's functions for static deformation and contain the mechanical properties such as Young's modulus and Poisson's ratio and the integrals are calculated in a finite-part sense [*Zhang et al.*, 2009].

2.3 Friction law

[22] As stated above, we do not consider fault strength variations caused by GCs surface characteristics. Instead, if fluid pressure and normal traction change because of the existence of GCs, the fault strength varies. For an equilibrium fault, the shear traction τ should be less than this fault strength everywhere. The fault strength τ_s, which obeys the cohesionless Coulomb friction law over the whole system, is equal to the product of the effective normal stress, i.e., σ_n-*p*, and the coefficient of friction, *f*, defined as

$$\tau_s=f(\sigma_n-p) \tag{3}$$

where the normal traction, σ_n, is thus not a constant, but evolves as part of the solution to the coupled boundary-value problems associated with the non-planar geometrical heterogeneities.

[23] The following truncated linear slip-weakening friction law is applied to the whole system including GCs, as in previous studies [*Uenishi and Rice*, 2003; *Garagash and Germanovich*, 2012). The coefficient of friction, *f*, is given by

$$f=\begin{cases} f_s & \text{if } u=0 \\ f_s-\dfrac{f_s-f_d}{u_c}|u| & \text{if } 0<|u|\le u_c \\ f_d & \text{if } |u|>u_c \end{cases} \tag{4}$$

where f_s and f_d are static and residual coefficients of friction, respectively, and u_c is the critical slip distance for which the coefficient of friction has been linearly reduced to its residual value.

[24] The choice of values for static and residual coefficients of friction, assumed to be constant in the model, is based on small slip rate experimental results. Their values are set based on experimental results [*Byerlee*, 1978; *Uenishi and Rice*, 2003], and are taken here to be equal to 0.8 and 0.5, respectively. Actually, the difference in the static and sliding coefficients can provide a finite fracture toughness for slip nucleation along a fault in a fracture mechanics model [*Palmer and Rice*, 1973]. But a nonsingular stress in the slip zone is used here for modeling slip development along a fault. The critical slip distance is difficult to determine because of the lack of sufficient data and because its value varies significantly between experiments and field tests, as discussed by *Uenishi and Rice* [2003]. Considering an immature fault, it is chosen as 0.1mm in our computations, which is also within the range recommended by *Uenishi and Rice* [2003].

[25] Because f_d is chosen as 0.5, the applied shear stress (4 MPa) on the fault is less than the residual frictional strength $f_d\sigma_{yy}$ =5MPa. On a flat fault, the slip process is stable if f_d >0.4 [*Garagash* and *Germanovich*, 2012]. We found that this conclusion is still valid in the presence of GCs even though some parts are opened by over-pressure. In the case of f_d =0.5, any faster slip rate obtained numerically is thus attributed to fault GCs. On the other hand, if the fault dilatant hardening attributed to surface roughness is considered, stable slow slip may occur when f_d <0.4 [*Zhang et al*., 2019; *Ciardo and Lecampion*, 2019].

[26] In addition, the points where the shear stress τ along a fault satisfies $|\tau| < \tau_s$ are defined to be in the sticking mode with no frictional slip occurring and for points that are in the sliding mode, we have $|\tau| = \tau_s$. The case of $|\tau| > \tau_s$ is not allowed. The slip motion also requires that $\tau \cdot \dot{u} \le 0$, where $\dot{u}$ is the slip rate, so that the slip increment has an opposite direction with respect to the frictional stress.

2.4 Fluid flow in the fault

[27] Fluid flow in the fault is assumed to be laminar, whether the fault is opened or closed, and the fault transmissivity is characterized by the well-known cubic law [*Tsang* and *Witherspoon*, 1981]. In plan strain, the volumetric flux per unit fracture thickness, $q(s,t)$, along the fault is defined based on Poiseuille's law as

$$q(s,t) = -\frac{(w+e)^3}{12\mu}\frac{\partial p}{\partial s} \tag{5}$$

where μ is the fluid viscosity, and $w+e$ is the total hydraulic aperture (or fault aperture). As the fault aperture is much smaller than the fault length, Poiseuille's law, which assumes a parallel flow channel, is a good approximation [*Tsang* and *Witherspoon*, 1981]. It is also taken as correct at fault intersections between segments where the fault width may change abruptly.

[28] The local mass balance condition for fluid flow in faults is

$$\frac{\partial w}{\partial t}+\frac{\partial q}{\partial s}=0 \tag{6}$$

[29] In the opened fault, substituting Eq. (5) into Eq. (6) leads to the well-known lubrication equation [*Detournay*, 2004]

$$\frac{\partial w}{\partial t}=\frac{\partial}{\partial s}\left[\frac{(w+e)^3}{12\mu}\frac{\partial p}{\partial s}\right] \tag{7}$$

[30] In the closed fault portions, we introduce the following relation to relax the fixed hydraulic aperture constraint [e.g., *Zhang et al.*, 2009]

$$\frac{\mathrm{d}e}{\mathrm{d}p}=\chi e \tag{8}$$

where χ is a small parameter with units of 1/Pa to represent fault contact compressibility.

[31] Based on mass balance, the above relaxation of the hydraulic aperture can lead to a diffusion-type equation for fluid pressure in the closed, but conductive fracture portion as [*Zhang et al.*, 2009]

$$\frac{\partial p}{\partial t}-\frac{\kappa}{e}\frac{\partial}{\partial s}(e^3\frac{\partial p}{\partial s})=0 \tag{9}$$

where $\kappa=1/(12\mu\chi)$.

[32] For forced fluid injection, the fluid front moves in time. The propagating velocity of the fluid front in a fault, $\dot{l}_f$, can be found in terms of $q(l_f,t)$ calculated from the upstream portion and the local fault aperture $w+e$ at the fluid front l_f as

$$\dot{l}_f=\lim_{s\to l_f^-}\frac{q(s,t)}{w(s,t)+e(s)} \tag{10}$$

[33] Because no fluid loss into the rock matrix is allowed, the constant injection rate means that the global mass balance reads

$$\sum_{i=1}^{N}\int_0^{l_f}(w+e)\mathrm{d}s = Q_0 t \quad (11)$$

where Q_0 is defined as the volumetric injection rate per unit fracture thickness with units of m^2/s under the plane strain condition.

2.5 Auxiliary conditions

[34] At the inlet, the constant injection rate is expressed as

$$q(0,t) = Q_0 \quad (12)$$

[35] At the slip front l_r, the shearing DD is zero and at the opening front l_o, the opening DD is zero, i.e.

$$w(l_o) = u(l_r) = 0 \quad (13)$$

[36] At segment intersections, the continuity of fluid mass is enforced and the induced pressure loss is negligible. Therefore, the fluid pressure must be the same for each fault segment end connected at the same intersection point [*Zhang et al.*, 2009]. In addition, the flow rate continuity is automatically enforced at the interface between the open and closed fault segments by satisfying the approximation given by Eq. (9).

[37] Initially, all pre-existing fault segments are assumed to contain no fluid, the rock mass is stationary, and an initial hydraulic aperture profile is assigned to each fault segment.

2.6 Numerical algorithm

[38] Numerical solutions to the above formulated problem are sought based on an implicit algorithm for iteratively solving the coupled equations for the pressure and deformation at a given time step as described previously by *Zhang et al.* [2009]. The fluid flux and pressure variations at intersection are incorporated in the solution process and the opening, slipping and fluid fronts are tracked by an external loop.

[39] For the elasticity equations, the DD-based boundary element method is used [*Crouch and Starfield*, 1983]. Discretization is made by using fixed-size constant-strength DD elements only along the fault segments, including branches, and en echelon and dilational sections.

[40] The flow equation for the fluid pressure in the fault, using either Eq. (7) or Eq. (10) depending on whether the fault segments are opened or closed, is solved for each time step by

means of a finite volume method (FVM). For closed fault segments, the evolution of e satisfies Eq. (8) with mass conservation imposed across the interface between the opened and closed segments upon solving Eq. (9). For opened fault segments, the combination of Eqs. (1, 2, 7) leads to an integro-differential equation for the fully coupled hydraulic fracture problem [*Zhang et al*., 2009]. It is solved by an iterative algorithm with the tolerance less than 10^{-14} on the relative errors of both fault opening and hydraulic aperture between two iteration steps.

[41] The convergence in friction modes is satisfied through one additional iteration outside the implicit iteration loop for the opening, hydraulic aperture and pressure [*Zhang et al*., 2009]. The numerical accuracy is controlled through global mass balance. Sometimes the solution requires a very small time step. Numerical results have been verified against some available theoretical and numerical results, including the high viscosity and no lag cases [*Zhang et al*., 2009; *Lecampion et al*., 2018]. The computations stop when the varying trends in slip and opening zones caused by GCs are clear or the effects of GCs are minimized. In the computations, the fault segment size outside all GCs is 8 m long so that the effects of GCs are captured before fluid and slip fronts approach the end of the meshed fault.

2.7 A verification case

[42] Prior to presenting numerical results, we provide the results for a special case, where an infinite straight fault is partially opened by fluid pressure to become a hybrid tension-shear fracture [*Blanton*, 1986]. *Blanton* [1986] provided the theoretical solution for fault-parallel normal stress σ_t as shown in Fig. 1 based on a given shear stress distribution to search for nucleation sites of new fractures on a sliding fault, but not for fault normal traction. A slip weakening process was not considered by *Blanton* [1986], therefore we use $f_s = f_d$. For this example, we set f_s=0.5 and σ_{yy}=10MPa.

[43] Along this straight extension-shear fault, the shear traction solely is responsible for generating the fault-parallel normal stress. In Blanton's model, the shear traction is specified to vary linearly from zero to the maximum $f_s\sigma_1$ (=5MPa) within the fluid-filled slipping zone. Our numerical result at a specified time under the same constraints, shown in Fig. 3, validates this linear variation hypothesis on the shear traction distribution used by *Blanton* [1986].

[44] Following the same notations in *Blanton* [1986], let us denote x as the distance from the inlet, such that x=s_1 is the opening front and x=s_2 is the slip front. The solution for the fracture-parallel normal stress σ_t at the position x, is given by *Blanton* [1986] as

$$\sigma_t = -\frac{f_s \sigma_1}{s_2 - s_1} V(x, s_1, s_2)$$

(14)

where the function $V(x, s_1, s_2)$ has the form of

$$V(x, s_1, s_2) = \frac{1}{\pi}\left[(x+s_1)\ln(\frac{x+s_2}{x+s_1})^2 + (x-s_1)\ln(\frac{x-s_2}{x-s_1})^2 + (s_2-s_1)\ln(\frac{x+s_2}{x-s_2})^2 \right]$$

[45] The fault-parallel normal stress distributions along the fault for a specified time instant, obtained numerically and based on Eq. (14), are both displayed in Fig. 3. Due to symmetry, numerical results are provided for only half of the fault. In Fig. 3, s_1=3.28m and s_2=4.56m and substituting these values into Eq. (14) provides the analytical solution of the fault-parallel normal stress. The numerical and analytical solutions agree reasonably well with each other in Fig. 3. The Blanton's solution thus provides another validation on our numerical model.

3. Numerical Results and Discussion

3.1 High permeability cracks

[46] Here, the term "cracks" refers to cavities or crack-like high-permeability zones on the fault plane. Their aperture is responsible for their permeability when closed, but does not change the stress field. The aperture affects the storage and movement of the injected fluids. Although these cracks can act as short-term fluid sinks, the downstream low-permeability fault section acts to reduce the rate at which fluid can leave the high-permeability crack zone. As injection continues, the increasing pressure in the crack zone will reach a value sufficient to open the downstream fault section, allowing the accumulated fluid volume contained by the cracks to move into the fault downstream. The growing fluid pressure zone may facilitate slip zone extension along the fault. This slip zone growth process would likely generate seismic events large enough to be recorded as seismic signals, as discussed by *Sibson* [2000]. Without loss of generality, a simple geometry shown in Fig. 2(a) is used to study the coupled response and slip rate variation associated with fluid flow and pressure interacting with these permeable crack zones. The material constants and the remote stresses are either given in Table 1 or are listed below. The crack cavity is modelled as an elliptic crack with a hydraulic aperture of 0.3mm at its mid-point and 0.01mm at the ends. The lowest hydraulic aperture is the same as that of the narrow fault connecting the cracks. In addition, for the results presented in this section, three different friction laws are used with the first two not including

a slip weakening process, i.e. $f_s = f_d$ =0.5 and 0.8, respectively and the third one including slip weakening in the form of f_s =0.8 and f_d =0.5.

[47] In calculation results not shown, we find that changes in the coefficient of friction do not alter the main features of slip development on the fault. Let us first consider the case of $f_s = f_d$ =0.5. Fig. 4 displays the along-the-fault distributions of opening, hydraulic aperture, slip and slip rate at two times, with x=0 corresponding to the fluid inlet and the five dots specifying the points A to E in Fig. 2(a). The hydraulic aperture change is extremely small during the fault deforming process and the locations of the two high-permeability cracks are obvious in the aperture curve. The opening and slip magnitudes increase with increasing time and injected fluid volume. The existence of the opening zone indicates that the fluid pressure at the crack mouth is above the background normal stress. The slip rate is very small at the two times shown due to the applied remote shear stress being less than the residual friction strength, but its history is very complex as discussed below. The maximum slip rate shown at two time instants is always located near the opening front. This is an important feature providing a means to track the opening zone in experiments and field tests, provided this slip rate generates detectable seismic signals.

[48] The opening, slip and pressure variations in time at Point A, B, C, D, and E are shown in Fig. 5 for the case of $f_s = f_d$ =0.8. The slip experiences an acceleration at two times when cracks 1 and 2 in Fig. 2(a) are pressurized and slip is re-initiated in their downstream fault segments, respectively. The faster slip occurs not only in the crack, but in the whole upstream area filled by fluids. The opening at point B starts at the same time as the faster slip as can be seen in Figs. 5(a) and (b). The faster slip may generate a relatively larger seismic event because of a larger moment rate produced over a fixed fault area. In addition, the existence of the permeable crack causes the slip to stop while the crack fills with fluid and is pressurized sufficiently to re-initiate slip. The re-initiation coincides with the pressure peak. However, it is rapidly followed by a pressure drop that results in a small decrease in opening at the injection point as seen in Figs. 5(c) and (a). The pressure drop is attributed to the enlargement of the pressurized segment, but the rate of pressure decrease is limited with opening soon resuming. The period of faster slip only occupies a small fraction of the overall process duration. This time interval provides a means to estimate the source size and the locations of high-permeability fault segments for the assumed fracture geometry as discussed in the previous studies for weak earthquake slips [*Boatwright*, 1984; *Urbancic* and *Trifu*, 1996].

[49] In Figs. 6(a-c), the changes in slip rates with time are displayed at the five specific locations for three choices of the coefficients of friction. As seen in Fig. 5(b), the transient peak slip rate occurs after a pause in slip. Such a spike occurs only once in Figs. 6(a) and (c), because the slip zone size becomes equal to the maximum fault size used in the computations or a larger value of f_d. This can be remedied by using a longer fault, but the major outcomes are the same. For example, there are two spikes in slip rate that coincide with the re-initiation of slip at the two cracks in Fig. 6(b). Moreover, the maximum slip rate is on the order of a few millimeters per second, much lower than the value typically taken as representing an earthquake slip rate. After the spikes, the slip rate is quickly reduced to less than 0.2 mm/s everywhere, which is in accordance with the stable slow slip requirement. In addition, the fault slip ceases along the entire fault while the fluid fills the permeable crack volume. The period when rupture propagation temporarily stops has been previously found for earthquake slips [*Imanishi et al*., 2004]. This silent or no-slip period provides another plausible method to obtain information about the fault geometry as argued by *Imanishi et al*. [2004]. If the fault geometry looks like Fig. 2(a), the stopping phase would suggest the location of fluid fronts.

[50] Figure 7 presents the variations in time of injection pressure and slip zone size for three choices of the coefficient of friction and a baseline case for a fault without high-permeability cracks. Injection pressure is independent of the coefficient of friction for the parameters used as shown in Fig. 7(a). This is because the slip and opening variations are decoupled for this planar fault geometry. Without cracks, a continuously decreasing injection pressure curve is found for the baseline case [*Detournay*, 2004]. However, there are small variations along the pressure curves when the fault trace contains cracks. The increase in the injection pressure occurs during the period of arrested slip zone growth as displayed in Fig. 7(b). After the slip is re-initiated, the injection pressure again tends to follow the baseline curve and the slip zone extends rapidly. One can see the match in time between the injection pressure peak and the faster growth in slip zone size. Interestingly, when the fluid enters a high-permeability crack zone, the injection pressure does not drop below the reference curve, but instead an increase in injection pressure is seen. This increase in pressure is attributed to the fluid filling of the crack zone that reduces the pressure level at the upstream of the crack to limit flow rate. Moreover, the second pressure bump for the case of f=0.8 at the time when the second pair of cracks are mechanically opened is much smaller than the first one. However, the time interval during which slip stops lasts longer. Thus, the duration of the

arrested slip phase may provide information that can be used to estimate the spacing of GCs or at least that multiple GCs exist, if the frictional behaviors and geometrical settings used in this paper can be applied to a real fault.

3.2 Dilational jogs

[51] Consider an along-the-fault section as shown in Fig. 2(b) with five flat steps and four identical dilational jogs subject to the applied shear stress that acts to assist in opening the jog by reducing the compressive stress acting across the jog. Mechanically, this stair-stepped geometry can generate fault conductivity change and slip deformation through the kinematic transfer of displacements between steps and jogs [*Sibson*, 1985, 1986; *Cox*, 1995; *Jeffrey et al*., 2009]. This kinematic transfer is dependent on the jog angle as shown in Fig. 2(b). The jog slip can only affect local permeability and slip on the step section within a short distance from the jog. The whole fault deformation can be considered as quasistatic and stable under the given stress states and injection rate because the perturbation to the contact stress caused by pressurizing the dilational jogs occurs slowly.

[52] For a jog angle of 30 degrees, the histories of opening, slip, slip rate and pressure at the specific five locations are displayed in Fig. 8, as well as the cumulative slip evolution. It should be noted that the maximum of the elliptic hydraulic aperture profile of the jog is w_0 =0.3mm, and the minimum at the jog ends is 0.01mm. The jogs remain fully closed throughout the time period shown in Fig. 8(a) and the conductivity resulting from the initial aperture is sufficient to allow transport of fluids. Using the labels in Fig. 2(b), jog 1 has been activated in slip, and its slip produces some opening along step 2 because of the kinematic transfer mechanism between jog and step. But jog 2 has not undergone slip by the end of the calculation, even though slip on the step 3 initiates, as found in Figs. 8(b) and 8(e). In addition, the slip value at point C exceeds that at point B. Therefore, the slip and opening on jog 1 are constrained by the step deformation. Moreover, as was found for the permeable cracks, the presence of dilational jogs slows down the slip development because there is an arresting phase for slip development as shown in Figs. 8(b) and (e). When the pressure is sufficient to initiate slip on both jog 1 and step 2, the slip on step 2 is accompanied by opening due to the kinematic transfer. This implies a rapid fracture volume increase that produces a reduction in pressure.

[53] The opening and pressure drops at point A signify the rapid increase in slip zone size as shown in Fig. 8(e) by the rapid expansion of slip zones as time increases from 4 to 6

seconds. The opening zone size also increases rapidly because step 2 is opened. The maximum slip rate occurs on the first jog and reaches 2.4 mm/s as shown in Fig. 8(c). Although this maximum is much smaller than the reference slip speed for small earthquakes, it may be associated with micro-earthquakes. Fig. 8(c) indicates that the slip rate at point A is large too and thus the larger peak slip rate spreads over the entire slip zone. The duration of the maximum slip speed is short. Afterwards, the slip speed quickly decreases to a much lower level at points A and B shown in Fig. 8(c). This implies stable slow slip zone growth with no detectable seismicity and progressive growth of the slip zone is shown in Fig. 8(e).

[54] The pressure variations at the five points are displayed in Fig. 8(d). As expected, the rapid fluid penetration after step 2 is opened directly results in a reduction of the injection pressure. This pressure drop also reflects the stress release over the fluid-filled region. The injection pressure level can drop below the confining stress for the steps (10 MPa). However, further drop is inhibited because the conductivity of steps is low and the area influenced by one slipping jog is small. After faster slip, the pressure difference is limited along the entire fluid zone.

[55] The variations of injection pressure and slip zone size in time are displayed in Fig. 9 for the three choices of the coefficients of friction. There is a slight increase in injection pressure before slip initiates at the first jog. In the same manner as cracks, this pressure increase is due to the filling of the permeable jogs. The faster slip zone growth is triggered by the buildup of fluid pressure. The slip zone extends faster for the case with a lower coefficient of friction as shown in Fig. 9(b). There is also a period of slip arrest for each case and its duration becomes shorter as the coefficient of friction is reduced. Implementing slip weakening increases duration of the arrest period, as shown in Fig. 9(b). This is because a lower value of f_d promotes slip zone growth, but initiation of slip on the steps is controlled by f_s.

[56] In addition to the coefficients of friction, slip development is also affected by the jog angle. In Fig. 10, only the jog angle is changed compared to the slip-weakening case in Fig. 8. Slip on the jogs does not occur and an intermittent slip pattern develops on the fault trace as shown in Fig. 10(a). The separated slip pattern has been recognized during shale gas stimulation [*Rutledge et al.,* 2004] and caldera formation eruption events [*Shelly et al*., 2016]. On the other hand, the maximum injection pressure occurring during generation of this slip pattern is higher than for the 30° jog angle case and approaches 12MPa as shown in Fig. 10(b). The non-slipping jog restricts opening of the downstream step for the fracture

geometry used. The narrow downstream steps and jogs result in this higher pressure.

3.3 Branches

[57] The fault branches are found to undergo the same kinematic transfer mechanism as the jogs. The non-planar branches can be activated in slip by the invading fluid and this slip imposes additional stresses across the neighboring fault portions of the branch through coherent deformation at the intersection. In addition, branches function as an alternative flow path [*Petit et al.*, 1999]. The selection of a new flow path can generate a slipping zone containing a change in slip orientation and magnitude.

[58] As depicted in Fig. 11(a), the slip re-orientation to the branch is evident. Here the branch angle shown in Fig. 2(c) is fixed as 45 degrees. Based on the stress condition shown in Fig. 2(c), the confining stress across the branches is 6MPa, much less than that across the main fault. When the fluid reaches the intersection, the branch becomes the preferred direction for fluid flow. Although a portion of fluid still follows the fault, this flow component is arrested eventually, as shown in Fig. 11(a). Note that the results obtained are based on the assumption that the branch length is sufficiently long so that fluid does not reach the tip of the branch to re-initiate fracture growth. This assumption is reasonable under some loading conditions. For example, the branch length can reach a size comparable to the main fault as discussed by *Barquins and Petit* [1992].

[59] The re-orientation of fluid flow into the branch can reduce the overall pressure level because the confining stress across the branch is lower. In Fig. 11(b), the pressure at point A keeps decreasing, but remains much higher than 6 MPa. As the fault hydraulic aperture is only 0.01mm, the pressure drop is limited because the pressure is found to be maintained above the confining stress acting across the fault, which results in some opening on the fault as the fluid flows toward and into the branch. Therefore, the injection pressure is dependent on the coupled process occurring upstream of branch 1.

[60] The fluid flow and slip re-orientation depend on the fault permeability when the branch angle is fixed. When the hydraulic aperture of the fault is increased from 0.01mm to 0.05mm, the slip zone on it is significantly enlarged as shown in Fig. 12(a). In contrast, the slip development in the branches is constrained and grows at a relatively lower speed. The slip magnitude at point E reaches the same level as that along branch 1 and it is zero on branch 2 using the labels in Fig. 2(c). The effect of the fault permeability on fluid invasion is evident in Fig. 12(b). The non-zero pressures at points D and E show that the fluid zone on the fault is longer than it was in Fig. 11(b). As these two points are both close to the second

fault-branch intersection, the fluid pressures at both locations are nearly identical. Therefore, by increasing the fault permeability, the fault becomes an important conduit to allow pressurized fluid to reach and enter more branches. The slip pattern may become more extensive and the larger slipping area may imply a relatively larger seismic event.

[61] Both fault permeability and coefficient of friction can affect the injection pressure in the presence of branches as shown in Fig. 13(a). At early time up to 4 seconds, the injection pressure increases with time from a lower level for a larger fault permeability (e=0.05mm), while it decreases with time for a small fault permeability (e=0.01mm) resembling a hydraulic fracture. This stage is insensitive to the coefficient of friction. However, the coefficient of friction plays a role later in combination with the fault permeability. When the coefficient of friction is higher, fluid flow along the fault to downstream of branch 1 becomes more difficult. This results in a lower injection pressure because the re-orientation process occurs with the slip being directed into branch 1. When the coefficient is lower, more energy is consumed for slip re-orientation because the injection pressure increases. In the presence of slip weakening, the injection pressure responses are similar to the case at the constant coefficient of friction equal to f_d.

[62] Figure 13(b) provides the slip zone size evolution, which helps in understanding the fault-branch competition in the case of a high-permeability fault. A lower coefficient of friction results in a larger and faster growing slip zone on the fault. The faster slip zone extension makes the long-term simulation difficult because a large number of elements would be needed to model the larger fault length required. The slip zone growth on branch 1 appears insensitive to the coefficient of friction. The slow fluid movement for f=0.8 and the rapid slip zone extension for f=0.5 on the fault can both reduce slip zone growth on branch 2. The slip weakening results in a relatively longer slip zone on branch 2, as shown in Fig. 13(b). Even in this case, the slip zone on branch 2 stops growing soon after initiating. Hence, it is difficult to create slip along all branches of a multi-branched fault system although higher fault permeability allows the pressurized fluid to enter more branches. For all cases studied, branch 1 plays an important role in slip and fluid flow re-orientation. The effect of downstream branches is less significant in the results obtained here, but a model that includes other factors such as finite-sized branches and permeability heterogeneity is needed to complete the analysis of multiple branch growth.

4. Conclusions

[63] By using a hydraulic fracture model, we have, for a set of given geometrical and loading parameters, numerically studied the slip development and fluid migration along a fault that contains three types of GCs, namely (1) discrete aperture-enhanced cracks, (2) jogs and (3) branches. In each case studied, the GCs, which exist on the meter scale, are given the same frictional and hydraulic properties and their heterogeneities on finer scales are not considered. In addition, the stress conditions are chosen so that aseismic stable slip becomes dominated over the slip process for all cases studied and the quasistatic stress analysis results are acceptable. The numerical results for three geometries used provide insights in better understanding the processes involved in generating microearthquakes as observed during hydraulic fracturing treatment of low-permeability reservoirs, for cases involving injection into faults containing pre-existing GCs. The linkage between slip development and fault permeability change induced by GCs has been highlighted by the transition between slow stable slipping and relatively faster rupturing.

[64] The impacts that the three types of GCs studied have on slip development are not exactly the same. The cracks and dilational jogs, when pressurized by injected fluid, can temporarily stop slip development or rupture propagation, which results in a short period of arrested slip. However, the arrested slip is followed by a subsequent faster slip phase. This rapid re-initiation of slip results in a detectable pressure drop. The faster slip rate and pressure drop are repeated, but with reduced magnitudes, at the next complexity position along the fault. The jog angle also plays a role in altering the slip patterns. When the jog is normal to the main fault or step direction, the slip zone is divided into parts by the jogs because the slip is inhibited on the right-angle jogs. On the other hand, for the case of a fault containing branches, the branches do not generate faster slip or a pressure drop. Instead, the slip zone propagation direction can be diverted into the branch. This re-orientation process is significantly affected by the main fault permeability.

[65] Care should be taken in applying these results to specific measurements at field sites because the measurements available at the seismic event locations are complicated and all parameters required to complete an analysis are not known. The results presented here obtained under the specified fracture geometries at the meter-scale, and using simplified stress, frictional and hydrological parameters. As such, only general patterns of seismic responses can been found and used to compare the numerical results presented to field cases. In addition, it must be noted that natural faults and fractures are of multi-scale natures and do

not possess uniform frictional properties as used in this model. The fault surface roughness and frictional strength heterogeneity at centimeter scale can influence slip zone growth on meter scale [*Zielke et al*. 2017; *Ye and Ghassemi*, 2018]. Furthermore, the direct comparisons of numerical results with measurements of carefully-designed experiments [*Lockner and Byerlee*, 1977; *Lei et al.*, 2000] are required. The fluid-driven shear tests on rough fractures in a lab scale by *Ye and Ghassemi* [2018] gave results with many features similar to those presented here. For examples, the aseismic slip accompanied by fault dilation, the correlation of stress drop and fast slip and the stick-slip behavior of the fault, due to the self-propping of asperities that are similar to the jogs at a finer scale, were found in the experiments.

Acknowledgements

We thank Associate Editor and two anonymous reviewers for their suggestions on plot quality and comments on inaccurate statements. XZ acknowledges the financial support of the Open Research Fund of State Key Laboratory of Geomechanics and Geotechnical Engineering, Institute of Rock and Soil Mechanics, Chinese Academy of Sciences, for his visit to the institute. DY and WC thank the support of the National Natural Science Foundation of China (Grant No: 51879260, 51879258). As per AGU's Data Policy, data for the plots in this paper can be accessed from CloudStor File Sharing and Storage Service (www.aarnet.edu.au).

References:

Aki, K., Fehler, M., & Das, S. (1977). Source mechanism of volcanic tremor: fluid-driven crack models and their application to the 1963 Kilauea eruption. *Journal of Volcanology and Geothermal Research*, 2, 259–287.

Azad, M., Garagash, D. I., & Satish, M. (2017). Nucleation of dynamic slip on a hydraulically fractured fault. *J. Geophys. Res: Solid Earth*, 122, 2812–2830,9.

Bao, X., & Eaton, D. W. (2016). Fault activation by hydraulic fracturing in western Canada. *Science*, 354, 1406–1409

Barquins, M. & Petit, J.-P. (1992). Kinetic instability during the propagation of a branch crack: Effects of loading conditions and internal pressure, *J. Struct. Geology* 14, 893-903.

Blanpied, M. L., Lockner, D. A., & Byerlee, J. D. (1993). An earthquake mechanism based on rapid sealing of faults. *Nature*, 362, 618–621

Blanton, T. L. (1986). Propagation of hydraulically and dynamically induced fractures in naturally fractured reservoirs. In *Unconventional Gas Technology Symposium*. Louisville, KY.

Boatwright, J. (1984). The effect of rupture complexity on estimates of source size. *J. Geophys. Res*, 89, 1132–1146.

Byerlee, J. (1978). Friction of rocks. *PAGEOPH*, 116, 615–626.

Caine, S. J., Evans, J. P., & Forster, C. B. (1996). Fault zone architecture and permeability structure. *Geology*, 24, 1025–1028.

Ciardo, F., & Lecampion, B. (2019). Effect of dilatancy on the transition from aseismic to seismic slip due to fluid injection in a fault. *J. Geophys. Res. Solid Earth*. 124, 3724–3743.

Cooke, M. L. (1997). Fracture localization along faults with spatially varying friction. *J. Geophys. Res*., 102, 22425–22434.

Cox, S. F. (1995). Faulting process at high fluid pressures: An example of fault valve behavior from the Wattle Gully Fault, Victoria, Australia. *J. Geophys. Res*, 100, 12841–12859.

Crouch, S. L., & Starfield, A. M. (1983). Boundary element method in solid mechanics, Allen & Unwin: London.

Das, I., & Zoback, M. D. (2013). Long-period long-duration seismic events during hydraulic stimulation of shale and tight-gas reservoirs — Part 1: Waveform characteristics. *Geophysics*, 78, KS97-KS108. https://doi.org/10.1190/1.3609093

Ellsworth, W. L. (2013). Injection-Induced Earthquakes. *Science*, 341, 1225942–1225942. https://doi.org/10.1126/science.1225942

Galis, M., J. P. Ampuero, P. M. Mai & F. Cappa (2017) Induced seismicity provides insight into why earthquake ruptures stop, *Science Advances* 3,7528.

Garagash, D. I., & Germanovich, L. N. (2012). Nucleation and arrest of dynamic slip on a pressurized fault. *J. Geophys. Res: Solid Earth*, 117, 1–27.

Guglielmi, Y., Cappa, F., Avouac, J.-P., Henry, P., & Elsworth, D. (2015). Seismicity triggered by fluid injection – induced aseismic slip. *Science*, 348, 1224–1227.

Hubbert, M. K., & William, W. R. (1959). Role of fluid pressure in mechanics of overthrust faulting: I Mechanics of fluid-filled porous solids and its application to overthrust faulting. *Bulletin of the Geological Society of America*, 70, 115–166.

Ida, Y. (1972). Cohesive force across the tip of a longitudinal shear-crack and Griffith's specific surface energy. *J. Geophys. Res*, 77, 3796–3805.

Imanishi, K., Takeo, M., Ellsworth, W. L., Ito, H., Matsuzawa, T., Kuwahara, Y., Ohmi, S. (2004). Source parameters and rupture velocities of microearthquakes in western Nagano, Japan, determined using stopping phases. *Bulletin of the Seismological Society of America*, 94, 1762–1780.

Jeffrey, R. G., Zhang, X., & Thiercelin, M. (2009). Hydraulic fracture offsetting in naturally fractured reservoirs: Quantifying a long-recognized process. In: *Proceedings of SPE Hydraulic Fracturing Technology Conference.*

Lapusta, N., Rice, J. R., Ben-Zion, Y., & Zheng, G. (2000). Elastodynamic analysis for slow tectonic loading with spontaneous rupture episodes on faults with rate- and state-dependent friction. *J. Geophys. Res*, 105, 23765-23789.

Lecampion, B., Bunger, A. & Zhang, X. (2018) Numerical methods for hydraulic fracture propagation: a review of recent trends, *Journal of Natural Gas Science and Engineering*, 49, 66-83.

Lei, X., Kusunose, K., Rao, M. V. M. S., Nishizawa, O., & Satoh, T. (2000), Quasi-static fault growth and cracking in homogeneous brittle rock under triaxial compression using acoustic emission monitoring, *J. Geophys. Res*., 105, 6127 – 6139,

Lockner, D., & Byerlee, J. D. (1977). Hydrofracture in Weber sandstone at high confining pressure and differential stress. *J. Geophys. Res.*, 82, 2018–2026.

Marone, C., Hobbs, B. E., & Ord, A. (1992). Coulomb constitutive laws for friction: contrasts in frictional behavior for distributed and localized shear. *PAGEOPH*, 139, 195–214.

McClure, M. W., & Horne, R. N. (2011). Investigation of injection-induced seismicity using a coupled fluid flow and rate/state friction model. *Geophysics*, 76, WC181-WC198.

Phillips, W. J. (1972). Hydraulic fracturing and mineralization, *J. Geol. Soc. Lond*. 128, 337-359.

Rutledge, J. T., Phillips, W. S., & Mayerhofer, M. J. (2004). Faulting induced by forced fluid injection and fluid flow forced by faulting: An interpretation of hydraulic-fracture microseismicity, Carthage Cotton Valley gas field, Texas. *Bulletin of the Seismological Society of America*, 94, 1817–1830.

Segall, P., & Pollard, D. D. (1983). Nucleation and growth of strike slip faults in granite. *J. Geophys. Res*, 88, 555–568.

Shapiro, S. A., Dinske, C., & Rothert, E. (2006). Hydraulic-fracturing controlled dynamics of microseismic clouds. *Geophysical Research Letters*, 33, 1–5.

Shelly, D. R., Ellsworth, W. L., & Hill, D. P. (2016a). Fluid-faulting evolution in high definition: Connecting fault structure and frequency-magnitude variations during the 2014 Long Valley Caldera, California, earthquake swarm. *J. Geophys. Res*: *Solid Earth*, 121, 1776–1795.

Shelly, D. R., Hardebeck, J. L., Ellsworth, W. L., & Hill, D. P. (2016b). A new strategy for earthquake focal mechanisms using waveform- correlation-derived relative polarities and cluster analysis: Application to the 2014 Long Valley Caldera earthquake swarm. *J. Geophys. Res. Solid Earth*. 121, 8622-8641,

Shelly, D. R., Hill, D. P., Massin, F., Farrell, J., Smith, R. B., & Taira, T. (2013). A fluid-driven earthquake swarm on the margin of the Yellowstone caldera. *J. Geophys. Res: Solid Earth*, 118, 4872–4886.

Sibson, R. H. (1985). Stopping of earthquake ruptures at dilational fault jogs. *Nature*, 316, 248–251.

Sibson, R. H. (1986). Earthquakes and lineament infrastructure. *Phil. Trans. R. Soc. Lond*. A, 317,

63–79.

Sibson, R. H. (2000). Fluid involvement in normal faulting. *Journal of Geodynamics*, 29, 469–499.

Šílený, J., Hill, D. P., Eisner, L., & Cornet, F. H. (2009). Non-double-couple mechanisms of microearthquakes induced by hydraulic fracturing. *J. Geophys. Res*: Solid Earth, 114, 1–15.

Tsang, Y. W., & Witherspoon, P. A. (1981). Hydromechanical behavior of a deformable rock fracture subject to normal stress. *J. Geophys. Res.*, 86, 9287–9298.

Uenishi, K., & Rice, J. R. (2003). Universal nucleation length for slip-weakening rupture instability under nonuniform fault loading. *J. Geophys. Res.*, 108, 2042.

Urbancic T., & Trifu, C.-I. (1996). Effects of rupture complexity and stress regime on scaling relations of induced microseismic events. PAGEOPH, 147, 319–343.

Viesca, R. C., & Rice, J. R. (2012). Nucleation of slip-weakening rupture instability in landslides by localized increase of pore pressure. *J. Geophys. Res*: Solid Earth, 117, 1–21.

Waite, G. P., & Smith, R. B. (2002). Seismic evidence for fluid migration accompanying subsidence of the Yellowstone caldera. *J. Geophys. Res*, 107, 2177.

Warpinski, N. R. (2014). A Review of Hydraulic-Fracture Induced Microseismicity. In: *48th US Rock Mechanics/Geomechanics Symposium*, ARMA 14-7774.

Wibberley, C. A. J., & Shimamoto, T. (2002). Internal structure and permeability of major strike - slip fault zones: The median tectonic line in Mie Prefecture, southwest Japan. *Journal of Structural Geology*, 25, 59 – 78.

Yamashita, T. (1997). Mechanical effect of fluid migration on the complexity of seismicity. *J. Geophys. Res.*, 102, 797 – 806.

Ye, Z., & Ghassemi, A. (2018). Injection-induced shear slip and permeability enhancement in granite fractures. *J. Geophys. Res. Solid Earth*, 123, 9009–9032.

Zielke, O., Galis, M. & Mai, P. M. (2017), Fault roughness and strength heterogeneity control earthquake size and stress drop, *Geophys. Res. Lett.*, 44, 777–783.

Zhang, F., Damjanac, B. & Maxwell, S. (2019), Investigating Hydraulic Fracturing Complexity in Naturally Fractured Rock Masses Using Fully Coupled Multiscale Numerical Modeling, *Rock Mech Rock Eng*., In press.

Zhang, X., & Jeffrey, R. G. (2014). Role of overpressurized fluid and fluid-driven fractures in forming fracture networks. *Journal of Geochemical Exploration*, 144, 194–207.

Zhang, X., & R. G. Jeffrey (2016). Fluid-driven nucleation and propagation of splay fractures from a permeable fault, *J. Geophys. Res. Solid Earth*, 121, 5257 – 5277.

Zhang, X., Jeffrey, R. G. & He, C. (2019) A numerical model for the effect of permeability change on faulting during fluid injection, *J. Geophys. Res*: *Solid Earth*, 124, 2080-2101.

Zhang, X., Jeffrey, R. G., & Thiercelin, M. (2009). Mechanics of fluid-driven fracture growth in naturally fractured reservoirs with simple network geometries. *J. Geophys. Res*, 114, 1–16.

Zimmerman, R. W., & Bodvarsson, G. S. (1996). Hydraulic conductivity of rock fractures. *Transport in Porous Media*, 23, 1–30.

Zoback, M. D., Kohli, A., Das, I., & Mcclure, M. (n.d.). The importance of slow slip on faults during hydraulic fracturing stimulation of shale gas reservoirs. In *American Unconventional Resources Conference*, SPE 155476. Pittsburgh, Pennsylvania.

Table 1 Typical model notations, definitions and values in the model

Symbol	Definitions	Value	Unit
a	Segment size for cracks and jogs	0.4	m
b	Branch size	∞	m
c	Spacing of dilational segments	4	m
d	Distance of the point on the branch to intersection	1	m
e	Hydraulic aperture	0.01-0.5	mm
f	Coefficient of friction	0.5-0.8	
f_s	Static coefficient of friction	0.8	
f_d	Dynamic coefficient of friction	0.5	
l_f	Distance of fluid front to inlet		m
l_o	Distance of opening front to inlet		m
l_r	Distance of slipping front to inlet		m
p	Fluid pressure		MPa
q	Volumetric flux		m^2/s
u	Shear displacement discontinuity		mm
u_c	Critical slip magnitude	0.1	mm
w	Opening displacement discontinuity		mm
E	Young's modulus	5	GPa
Q_0	Injection rate	0.0001	m^2/s
ν	Poisson's ratio	0.25	
χ	Fracture compressibility	10^{-8}	1/Pa
μ	Fluid viscosity	0.001	Pa·s
σ_n	Normal confining stress		MPa
τ	Frictional stress		MPa
σ_{xx}	Remote normal stress in x direction	10	MPa
σ_{yy}	Remote normal stress in y direction	10	MPa
σ_{xy}	Remote shear stress	4	MPa
σ_1	Remote maximum principal stress		MPa
σ_2	Remote minimum principal stress		MPa
σ_0	Resultant normal stress by remote principal stresses		MPa
τ_0	Resultant shear stress by remote principal stresses		MPa
τ_s	Fault strength		MPa
θ	Jog angle or branch angle		degree

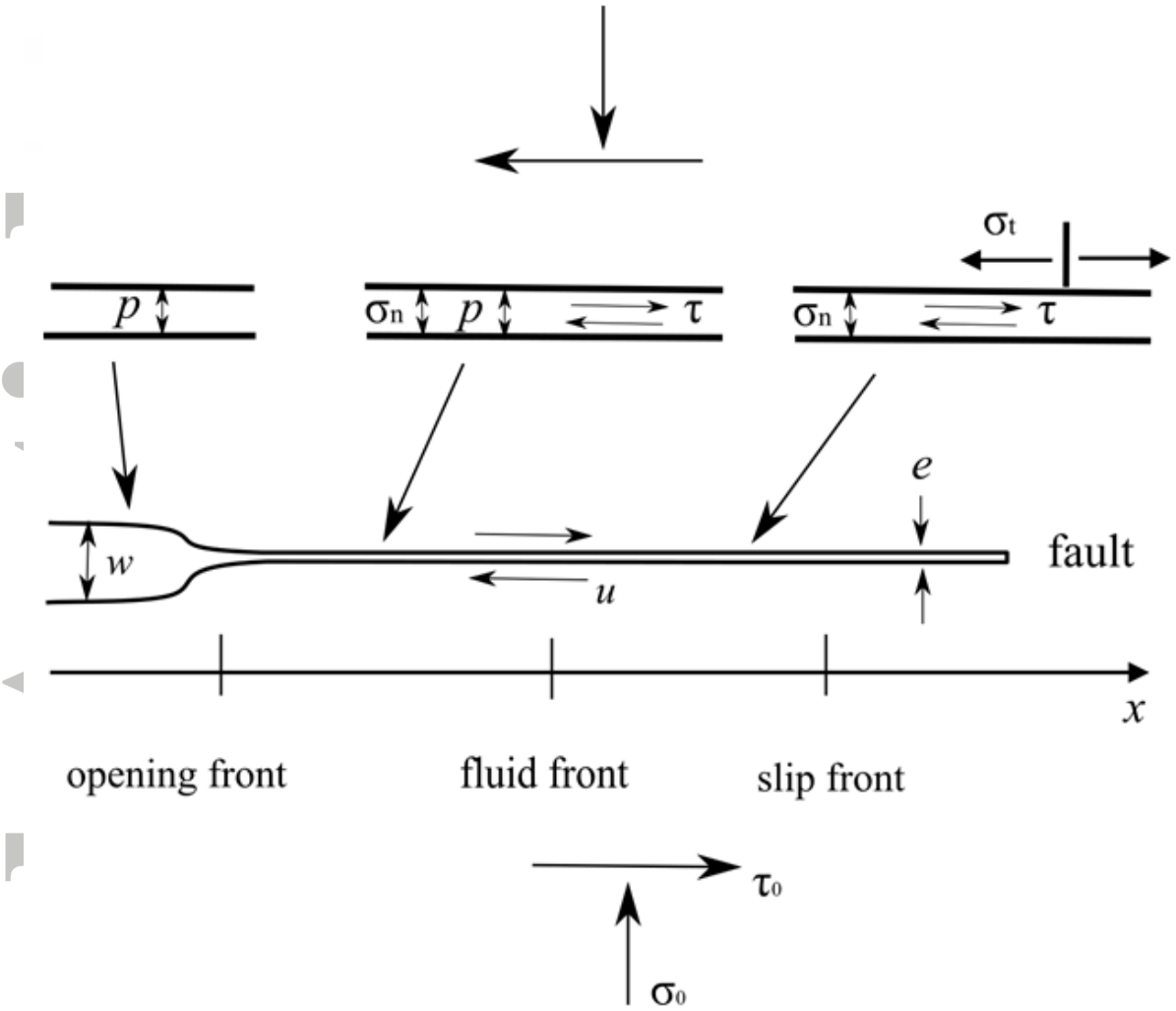

Figure 1. Schematic of stress, deformation and flow states in the open zone with opening w>0, the pressurized zone with pressure p>0 and the slip zone with slip displacement u>0 along the fault lying on the x-axis. These three zones can co-exist and possess different permeabilities. For example, the hydraulic aperture e conveys fluids if the opening w=0. There are three corresponding moving fronts (opening, fluid-filled, and shearing), whose order may differ depending on fluid movement. The far-field or remote stresses act to generate background normal (σ_0) and shear (τ_0) stresses and the normal and tangential tractions on the fault are denoted by σ_n and τ. The fault slip can generate an extensional fault-parallel normal stress (σ_t) along the top surface of the fault. The stress, deformation and flow states are also applicable to non-planar fracture systems.

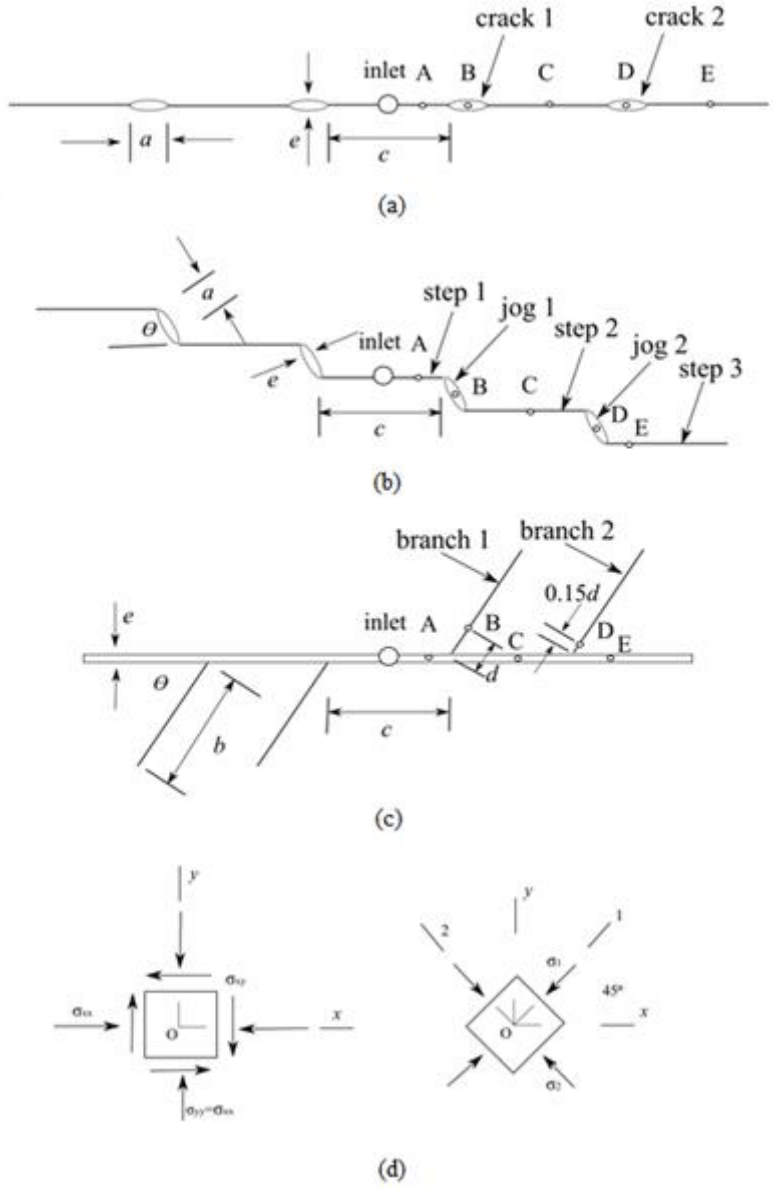

Figure 2. Description of three fault GCs, (a) cracks; (b) dilational jogs; and (c) branches, on both sides of the inlet. *c* is the distance between two complexities. The size of the dilational segments is *a* and the branch length is *b*. The out-of-fault plane angles are denoted by θ in (b) and (c). Due to geometrical symmetry, only the complexities on the right-hand side of the inlet are labelled based on the distance to the inlet. Five points labeled A, B, C, D, and E are specified for locations where numerical results are reported in subsequent figures. (d) The remote stresses and principal stresses and the coordinate systems are shown.

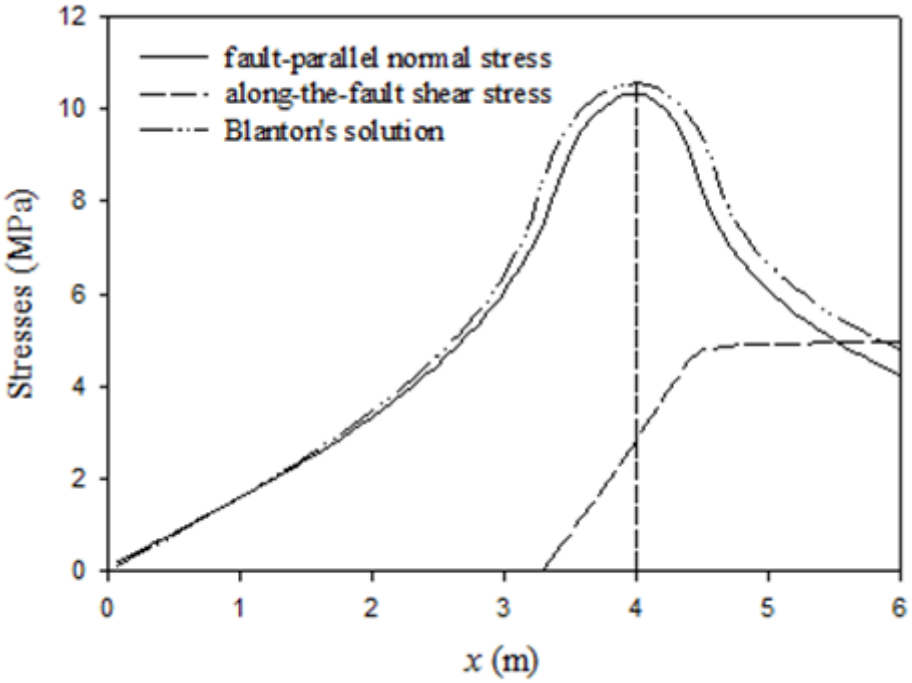

Figure 3. Distributions of fault-parallel normal stress along the top of the fault surface obtained by this model and by *Blanton* [1986] and distributions of the shear stress along the fault obtained by this model at a specified time.

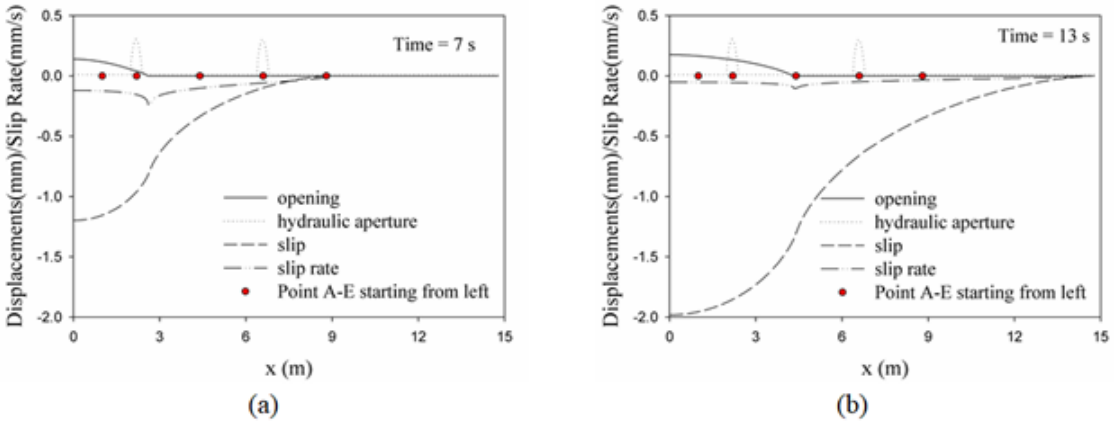

Figure 4. Distributions of along-the-fault opening, hydraulic aperture, slip and slip rate at two times (a) t=7 s and (b) t=13 s for the case of $f_s = f_d$ =0.5. The filled circles signify the locations for Points A, B, C D, E from left to right as given in Fig. 2(a).

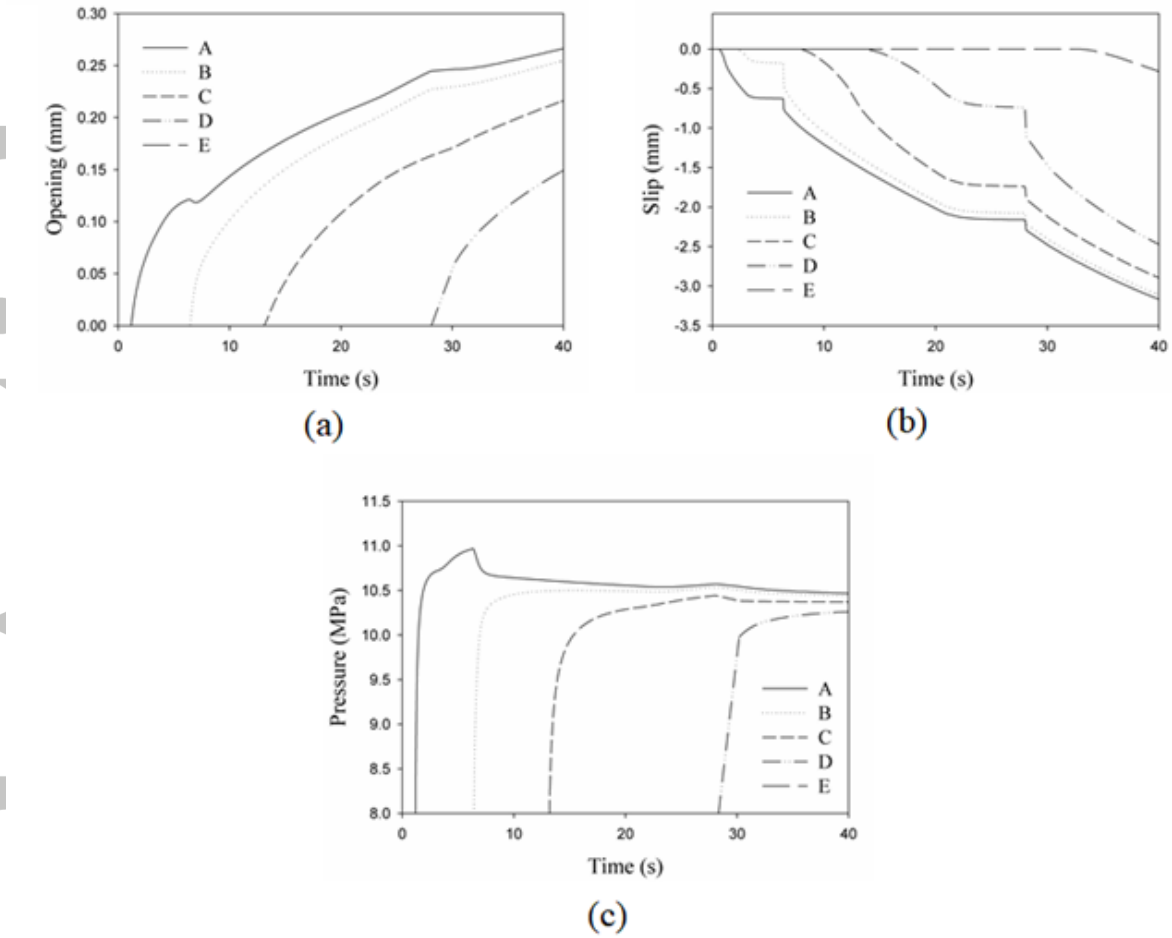

Figure 5: Variation along the fault of (a) opening (b) slip and (c) pressure with injection time at the five specific locations shown in Fig. 2(a) for the case of $f_s=f_d=0.8$.

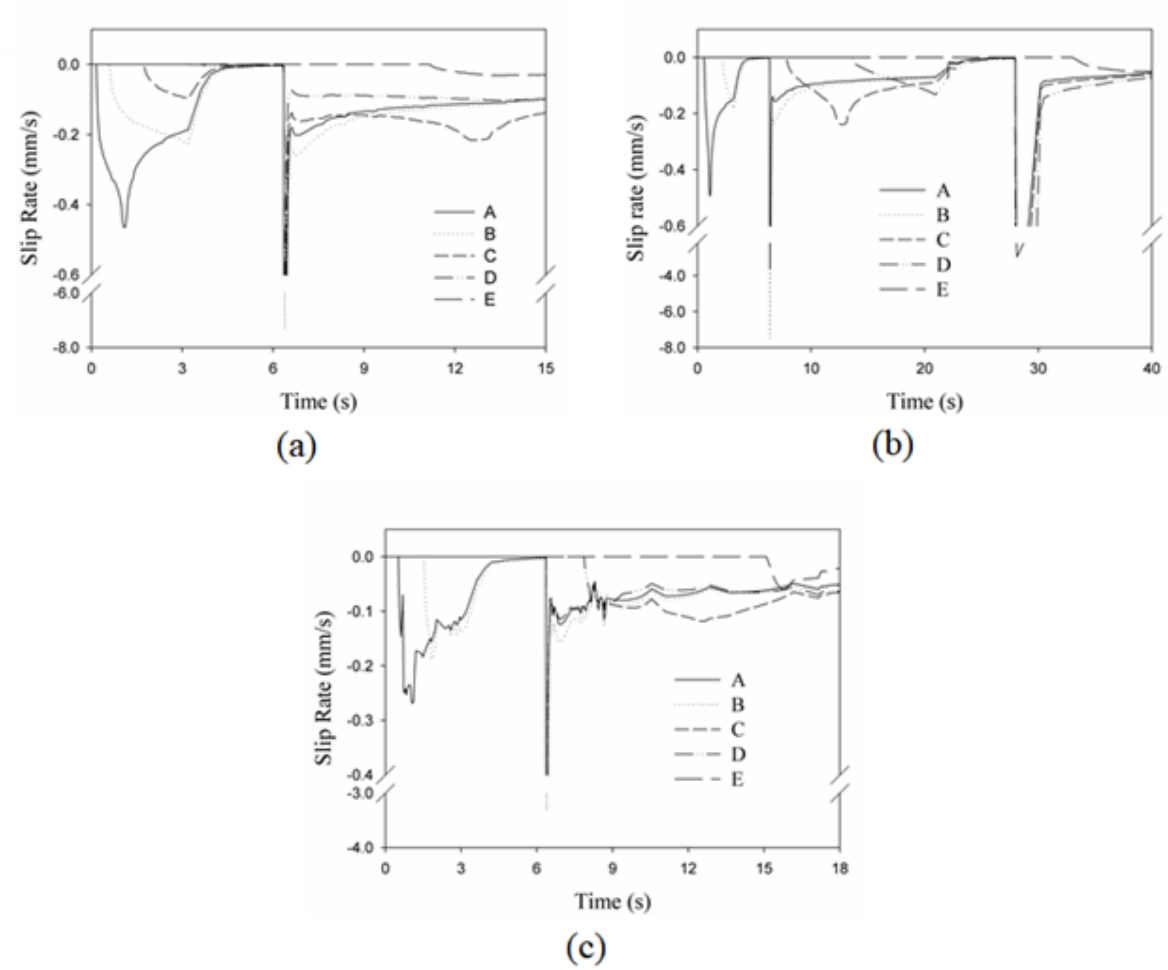

Figure 6. Time-varying slip rates at the five specific positions shown in Fig. 2(a) for the cases of (a) $f_s = f_d$ =0.5, (b) $f_s = f_d$ =0.8 and (c) f_s =0.8 and f_d =0.5.

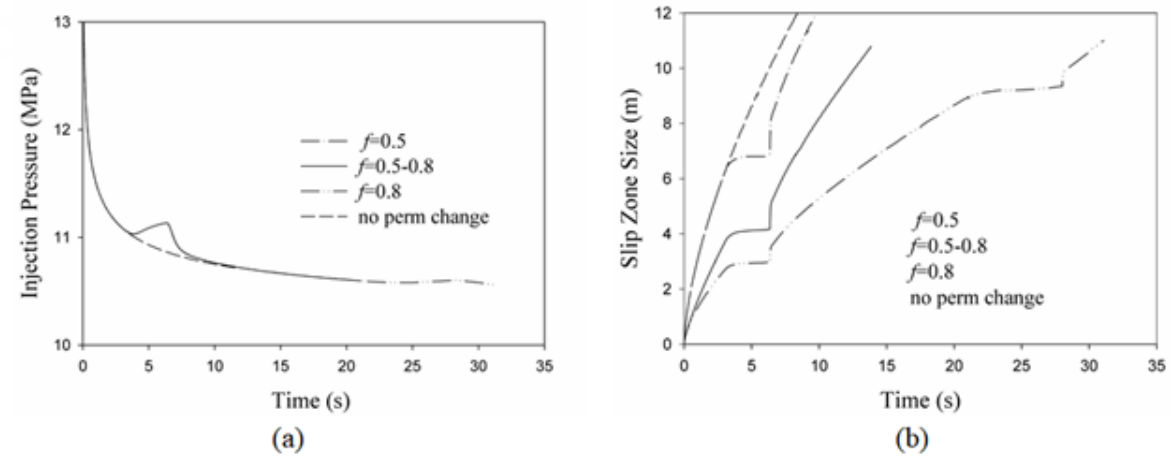

Figure 7. Time-varying injection pressures (a) and slip zone sizes (b) for different choices of the coefficients of friction. A reference case without cracks and for f=0.5 is also provided.

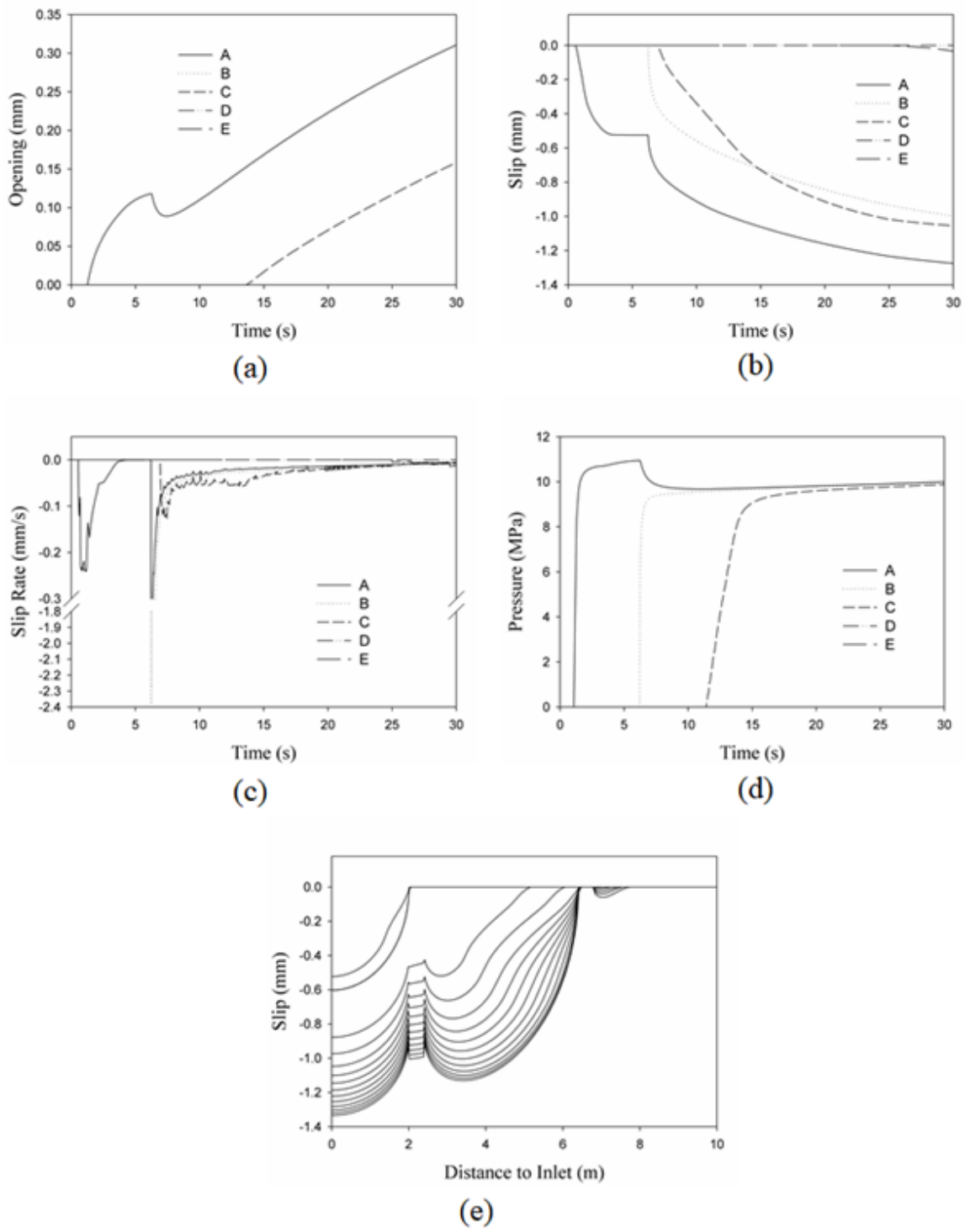

Figure 8. Time dependent (a) opening, (b) slip, (c) slip rate and (d) pressure at the five specified locations shown in Fig. 2(b) and (e) accumulation of slip vs the distance to the inlet along the fault patch at every 2 seconds for the case of f_s =0.8 and f_d =0.5 when the jog angle is equal to 30 degrees. The locations of five specified points can be found in Fig. 2(b).

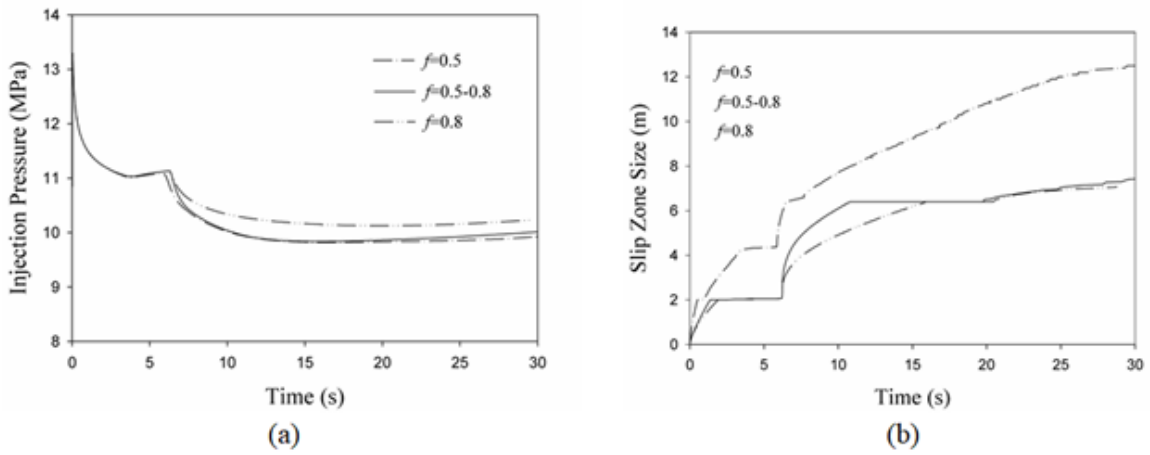

Figure 9. Time-varying injection pressures (a) and slip zone sizes (b) for different choices of coefficients of friction for a jog angle of 30 degrees.

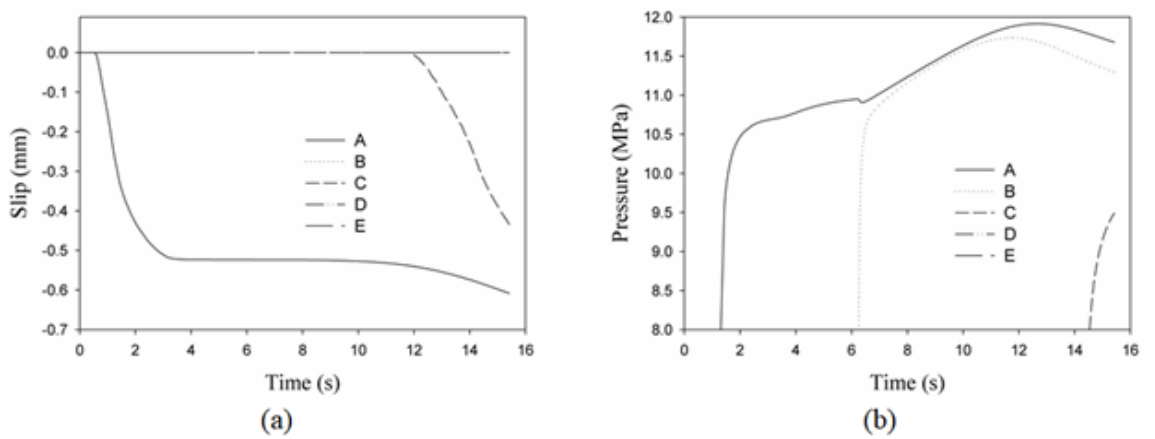

Figure 10. Variations in time of (a) slip and (b) pressure at the five specified locations for the case of f_s=0.8 and f_d=0.5 for a jog angle of 90 degrees. The locations of the five specified points can be found in Fig. 2(b).

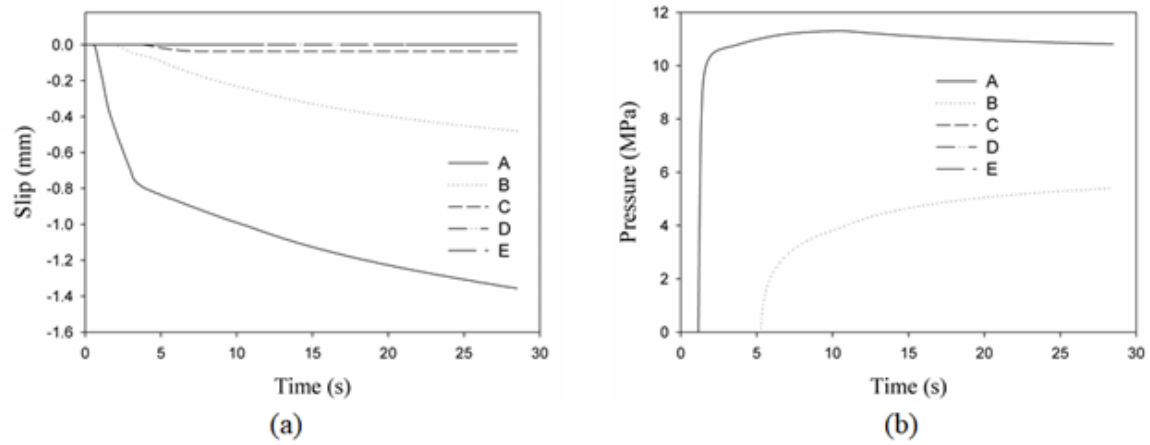

Figure 11. Variations in time of along-the-fault (a) slip and (b) pressure at the five specific locations shown in Fig. 2(c) for the case of f_s =0.8 and f_d =0.5 when the initial fault hydraulic aperture *e*=0.01mm. The confining normal stress across the branches is 6MPa. The locations of the five specified points can be found in Fig. 2(c).

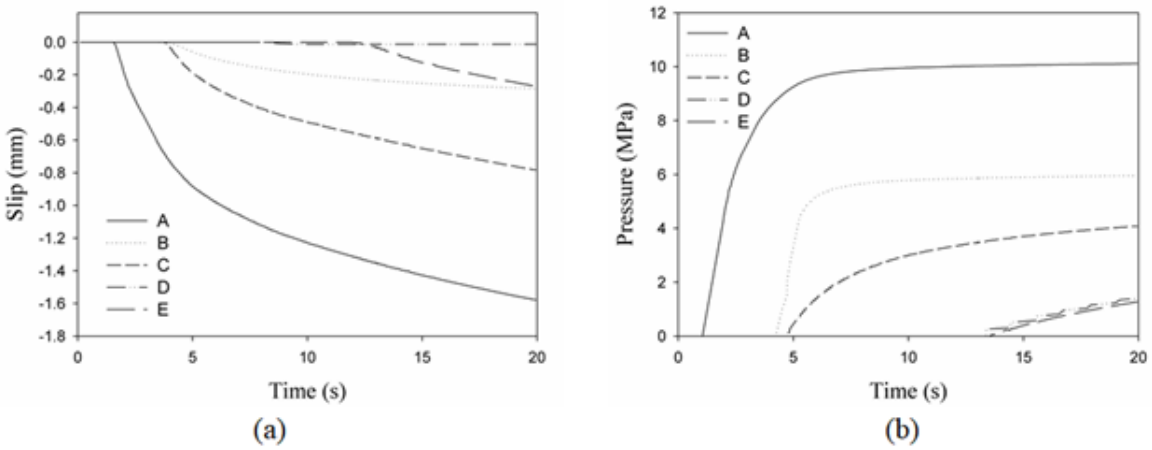

Figure 12. Variations in time of (a) slip and (b) pressure at the five points along the fault-branch system in the case of f_s=0.8 and f_d=0.5 when the initial fault hydraulic aperture is 0.05mm. The locations of five specified points can be found in Fig. 2(c).

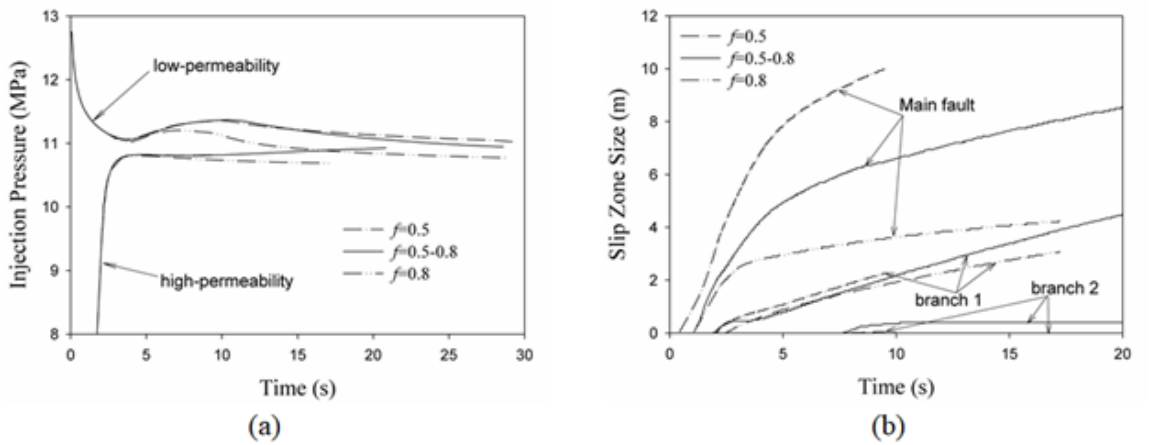

Figure 13. (a) Time-dependent variations of injection pressure for several values of the coefficient of friction for a high-permeability case (e=0.05mm) and a low-permeability case (e=0.01mm). (b) Variations of slip zone sizes with time for several values of the coefficient of friction for a high-permeability case (e=0.05mm).